Supporting Information for 'Narrow, fast, and "cold" mantle plumes caused by strain-weakening rheology in Earth's lower mantle'

Anna J. P. Gülcher[1], G. J. Golabek[2], M. Thielmann[2], M. D. Ballmer[3], and P. J. Tackley[1]

[1]Institute of Geophysics, Department of Earth Sciences, ETH Zurich, Zurich, Switzerland

[2]Bayerisches Geoinstitut, University Bayreuth, Bayreuth, Germany

[3]UCL Earth Sciences, University College London, London, UK

Contents of this file

Additional Supporting Information (Movie files uploaded separately)

This file contains Supporting Information Text S1-S4, Figures S1-S7, Tables S1 and S2, and the accompanying captions for movies S1-S5, which supplement the article 'Narrow, fast, and "cold" mantle plumes caused by strain-weakening rheology in Earth's lower mantle'.

Corresponding author: Anna Gülcher, Institute of Geophysics, Department of Earth Sciences, ETH Zurich, Zurich, Switzerland. (anna.guelcher@erdw.ethz.ch)

Text S1. Strain formulation

We have chosen to track deformation and apply weakening/healing in full tensor form, because this allows for incorporating full history-dependent deformation and strain. This is in contrast to various studies that just tracked the second invariant of strain rate (e.g., Tackley, 2000b; Fuchs & Becker, 2019). Tracking the deformation matrix (e.g. strain ellipse) also has many potentials for future research, including directional information of deformation related to mineral fabric, lattice-preferred orientation, and seismic anisotropy.

Several approaches provide a dimensionless measure of strain magnitude based on the shape of the strain ellipsoid (i.e., semi-major and -minor axes a and b, giving the maximum and minimum stretch), independently of its orientation. We chose to follow (McKenzie, 1979) by calculating the logarithmic strain ($\varepsilon_{log10} = log_{10}(a/b)$), which can be translated to the "natural strain" ($\varepsilon_{ln} = ln(a/b) = \varepsilon_{log10} \cdot ln(10)$) and the strain ellipse aspect ratio ($R = a/b = 10^{\varepsilon_{log10}}$). Figure S1 shows different projections of the same weakening profile used in this study using different finite strain definitions (horizontal axis). These different curves (same weakening behavior) highlight how the description of the temporal evolution of weakening is highly dependent on the formulation of strain applied.

Text S2. Rheological healing

Below, we detail the intermediate steps from eq. (4) to eq. (5) in the main paper.

$$\frac{dM}{dt} = -H \cdot (M - I) \tag{S1}$$

$$\frac{1}{M - I} dM = -H \cdot dt \tag{S2}$$

$$\int_{M_{\text{old}}}^{M_{\text{new}}} \frac{1}{M - I} dM = -H \cdot dt \tag{S3}$$

$$ln\left(\frac{M_{\text{new}} - I}{M_{\text{old}} - I}\right) = -H \cdot dt \tag{S4}$$

$$\frac{M_{\text{new}} - I}{M_{\text{old}} - I} = exp(-H \cdot dt) \tag{S5}$$

$$M_{\text{new}} - I = (M_{\text{old}} - I) \cdot exp(-H \cdot dt) \tag{S6}$$

$$M_{\text{new}} = M_{\text{old}} \cdot exp(-H \cdot \text{dt}) + I \cdot [1 - exp(-H \cdot \text{dt})] \tag{S7}$$

Where M_{new} is the updated deformation matrix, M_{old} is the deformation matrix before healing, dt is the time step in seconds, I is the unit matrix, and H is the rheological healing rate ($=\frac{1}{\tau_{\text{h}}}$ with reference timescale of rheological healing τ_{h}). This healing rate causes M to relax towards a unit matrix I.

Figure S2 shows healing-rate profiles based on eq. (6) in the main paper for several reference adiabats (T_0=1300, 1600 and 1900 K) as well as for the initial geotherm in our experiments.

The profiles show that rheological healing generally decreases with depth along an adiabat. On the other hand, healing is strongly temperature-dependent: healing significantly increases and decreases for temperatures hotter and cooler than the reference adiabat, respectively. The profile along the initial geotherm further shows that no significant healing is expected in the lithosphere or sinking slabs. Conversely, efficient healing should occur in anomalously hot plumes.

Final snapshots for models that differ only in the extent of imposed healing are shown in Figure S3. In these models, no strain-dependent weakening is applied. Rheological healing mainly occurs in the upper mantle ($T < 1600$ K) and relatively hot anomalies (upwellings) in the lower mantle. Cold anomalies (plates) remain unaltered by rheological healing. This affects the final strain pattern as well: for moderate healing (Fig. S3b,c), accumulated strain efficiently heals in the upper mantle as well as the narrow central conduits of the hot upwellings. Relatively warm areas around these hottest narrow conduits remain strained as they are not very efficiently healed. For fast healing (Fig. S3d), strain recovery is efficient, and only little strain is accumulated near upwellings as well as in subducted slabs in the upper mantle.

Text S3. Detection of mantle domains

We use the geodynamic diagnostics software StagLab (Crameri, 2018) to automatically detect regional flows that are either self-driven (i.e., active) or induced (i.e., passive). Active regional flows represent mantle plumes (active upwellings) or active slabs (active downwellings). Passive slab remnants in the mantle that are not actively sinking, are not detected in this routine. Many previous studies use either the temperature field (e.g., Labrosse, 2002) or the radial velocity field (e.g., Hassan et al., 2015) to detect mantle plumes in numerical mantle convection models. Yet using either such a thermal or dynamic definition does not work for our set of numerical models, as our modelled plumes significantly vary in terms of their anomalies in both temperature and radial velocity.

Here, we present our unique approach of identifying mantle plumes and slabs in our models, using a combined thermal-dynamical approach, which is newly implemented in the StagLab toolbox (Crameri, 2018), and can be found on https://github.com/annaguelcher/StagLab-OS.git. This approach analyses the temperature (T) and radial velocity field (v_z), and their horizontal residual fields T_{res} and $v_{\mathrm{z,res}}$, which are the normalised fields to the horizontal mean at each depth. These fields are combined into the residual radial heat advection, which is given as $T_{\mathrm{res}} \cdot |v_{\mathrm{z,res}}|$. Absolute values of $v_{\mathrm{z,res}}$ are used to make sure that the result is negative for cold downwellings and positive for hot upwellings. This parameter may be large for regions with an anomalously large T_{res} and/or an anomalously large $v_{\mathrm{z,res}}$ (i.e., both hot, slow upwellings and colder, fast upwellings). For the detection of plumes and slabs, the residual fields T_{res} and $T_{\mathrm{res}} \cdot |v_{\mathrm{z,res}}|$ at each time step are statistically analysed, and their percentiles $P_{\#}\{..\}$ are used for the definition

of the plume/slab thresholds. Mantle plumes are detected using the following conditions:

$$T_{\mathrm{res}} \geq P_{85}\left\{T_{\mathrm{res}}\right\} \tag{S9}$$

$$T_{\mathrm{res}} \cdot |v_{\mathrm{z,res}}| \geq P_{90}\left\{T_{\mathrm{res}} \cdot |v_{\mathrm{z,res}}|\right\} \tag{S10}$$

Where P_{85} and P_{90} are the 85^{th} and 90^{th} percentiles of the respective fields specified in the {} brackets. Slabs are detected using the following conditions:

$$T_{\mathrm{res}} \leq P_{15}\left\{T_{\mathrm{res}}\right\} \tag{S11}$$

$$T_{\mathrm{res}} \cdot |v_{\mathrm{z,res}}| \leq P_{10}\left\{T_{\mathrm{res}} \cdot |v_{\mathrm{z,res}}|\right\} \tag{S12}$$

Absolute cut-offs for minimum T_{res} and $T_{\mathrm{res}} \cdot |v_{\mathrm{z,res}}|$ are put to 50 K and ± 0.48 K cm yr^{-1} (as in Arnould et al., 2020). Once these plume and slab anomalies are located, they are checked for their connectivity using a classical image processing procedure searching for connected pixels in a matrix (Crameri, 2018, and references therein). Small anomaly areas are immediately removed (as in Crameri, 2018). Moreover, plumes in the mantle should have a minimum vertical extent ($d_z = 500$ km). The same holds for slabs in the lower mantle ($d_z = 400$ km), although this size threshold is ignored for newly-developing slab(lets) in the upper mantle, passing through a depth of 250 km.

We also detect passive up- and downwellings, that are, in contrast to the active regions defined above, flowing passively due to induced forces. These regions are defined as regions other than slabs or plumes, where the v_{z} value surpasses $1/100 \cdot \max\left(\mathrm{v_z}\right)$ (upwellings) or is lower than $1/100 \cdot \min\left(\mathrm{v_z}\right)$ (downwellings).

Finally, the mantle diagnostics routine also detects basaltic piles present at the core-mantle boundary (CMB). As internal convection usually occurs within these piles (see Results), any active upwelling (plume) detected within these piles are removed from the plume field, since this concerns a separate convecting system. The pile detection routine is based on composition and temperature: in terms of composition, pile material must consist of at least 60% of the pile must consist of basaltic material ($C_{\mathrm{bs}} \geq 0.6$). The temperature constraint is defined using the average of a mid-mantle temperature of 3000 K and the CMB temperature: $T \geq \left(3000 + T_{\mathrm{CMB}}\right)/2$ [K] (as in Schierjott et al., 2020).

Text S4. Additional SW models with similar final mantle viscosity profiles

models discussed in the main text display a distinct effective viscosity profile through time, which, in turn this strongly affects model evolution by itself. We ran five additional strain-weakening rheology cases with a higher intrinsic viscosity jump in the lower mantle ($\lambda_{660} > 10$), such that the final viscosity profiles of these cases are similar to that of the reference model M_0 (and to each other). This allows us to distinguish the direct (first-order) effects of SW

rheology on mantle dynamics from those of the radial viscosity profile (second-order effect of SW rheology). The outcomes of these additional cases are summarised in Table S2 and Figures S5-S7. Videos S4 and S5 show the time evolution of internal dynamics for two selected cases (those illustrated in Figures S6 and S7). Below follows a description of related results, ordered in a similar way as the discussion in the main text.

Global mantle convective patterns

Despite similar final mantle viscosity profile and average mantle viscosity within the ensemble of additional models and compared to the reference model M_0 (Fig. S5b), the convective vigour is still affected by SW due to localization of flow. The average values for v_{RMS} are $\sim$50% higher in the additional SW models than in the reference model case (see Table S2, Fig. S7b and Fig. 5 in the main paper). In particular, the v_{RMS} histogram is more skewed, with high values (> 2 cm/yr) for SW models, and hardly any such very high velocity domains for the reference case (Fig. S7b). Most of this increased mantle flow velocity is focused in the narrow, weakened upwelling regions (Fig. S7b,e) and Videos S4-S5). With this higher convective vigor, the patterns of mantle flow is also affected (see Fig. S6), but much less so relative to the corresponding SW rheology models with $\lambda_{660} = 10$ (see Fig. 6 in main text). While the length- and timescales of convection for our additional SW cases are much more similar to that of the reference case (M_0), SW rheology still causes the formation of narrower convection cells and more mantle plumes with shorter lifetimes (Fig. S6b-c). In terms of the distribution of the age of all mantle materials (Fig. S7c), the mean age of all mantle materials is indistinguishable between all cases, similar to our findings in the main text.

Thermal evolution

In addition to similar final mantle viscosity profiles, the additional cases also display roughly similar mantle thermal evolution and final average mantle temperatures (Fig. S5a). Top Nusselt numbers are fairly equal in all cases, whereas the bottom Nusselt numbers are still slightly increased in the additional SW rheology models (Fig. 5 in the main paper), however much less than in the related SW rheology models with $\lambda_{660} = 10$ (main paper). This strengthens our conclusion that CMB heat flux is preferentially accommodated via convection vs conduction due to SW in the lowermost mantle.

Thermochemical piles

Despite the whole-mantle viscosity being roughly equal between cases, basalt segregation is still more efficient in the additional SW rheology cases (Fig. S5c), and thermochemical piles formed in the lowermost mantle are still larger (Fig. S6; Table S1). Again, this strengthens our main conclusions.

Plume dynamics

Finally, in these additional cases, weakened mantle plumes are still significantly faster, narrower, and colder, than those in the reference case (Fig. S7d-f). In fact, the ratio of upwelling velocity

within the narrow mantle plumes over the average mantle-flow velocity is even much higher in these additional SW rheology cases compared to the corresponding SW models discussed in the main text.

Conclusions

Based on the outcomes above, we conclude that SW rheology is the critical ingredient for *(i)* weak and *(ii)* narrow plumes with *(iii)* relatively low thermal anomalies, as well as *(iv)* large and long-lived thermochemical piles. Secondary effects of SW rheology, such as on CMB heat flux and mantle cooling, are caused by its effects on mantle dynamics by increasing convective vigor (locally). At a fixed average lower-mantle viscosity, CMB heat flux and mantle thermal evolution is still affected by SW, but much less so than in our models in the main text.

Captions for Movies S1 to S5

Movie S1: Evolution of reference model M_0
Evolution of reference model M_0 (no strain weakening and no rheological healing, $\lambda_{660} = 10$) over 5 billion years of model time. The video consists of six panels, each showing a different field: **(a)** basalt fraction, **(b)** material age (time since material last underwent a melting episode), **(c)** temperature, **(d)** viscosity, **(e)** detected mantle domain field (see Text S3), and **(f)** strain field. The detailed discussion on the evolution of this model can be found in Section 3.1 of the main paper.

Movie S2: Evolution of model M_{001}
Evolution of model M_{001} ($f_{\mathrm{w}}^{\max} = 0.01$, no rheological healing, $\lambda_{660} = 10$) over 5 billion years of model time. The video consists of six panels, each showing a different field: **(a)** basalt fraction, **(b)** material age (time since material last underwent a melting episode), **(c)** temperature, **(d)** viscosity, **(e)** detected mantle domain field (see Text S3), and **(f)** strain field. In contrast to the reference model (Movie S1), the convective vigor is increased, thermochemical piles in the lowermost mantle are more stable, and mantle plumes are significantly narrower, colder, and more transient (see main paper).

Movie S3: Evolution of model $M_{01\mathrm{H16}}$
Evolution of model $M_{01\mathrm{H16}}$ ($f_{\mathrm{w}}^{\max} = 0.01$, $H_{660} = 10^{-16}$ s^{-1}, $\lambda_{660} = 10$) over 5 billion years of model time. The video consists of six panels, each showing a different field: **(a)** basalt fraction, **(b)** material age (time since material last underwent a melting episode), **(c)** temperature, **(d)** viscosity, **(e)** detected mantle domain field (see Text S3), and **(f)** strain field. Even though the strain field experienced more healing compared to pure SW models (such as Movie S2), the same type of changes in mantle flow, pile stability, and plume dynamics apply as for pure SW models (see main paper).

Movie S4: Evolution of model $M_{001\lambda}$
Evolution of model $M_{001\lambda}$ ($f_{\mathrm{w}}^{\max} = 0.01$, no rheological healing, $\lambda_{660} = 20$) over 5 billion years of model time. The video consists of six panels, each showing a different field: **(a)** basalt fraction, **(b)** material age (time since material last underwent a melting episode), **(c)** temperature, **(d)** viscosity, **(e)** detected mantle domain field (see Text S3), and **(f)** strain field. Even though SW rheology operates in the modelled lower mantle, the model shows a similar thermal evolution and final viscosity profile as the reference model M_0 (see Fig. S5) due to the increased viscosity jump in the lower-mantle (λ_{660}). Strain localization still occurs in mantle plumes and thermochemical piles, and their dynamics are different than those in the reference model (see Text S4).

Movie S5: Evolution of model $M_{01\mathrm{H16}\lambda}$
Evolution of model $M_{01\mathrm{H16}\lambda}$ ($f_{\mathrm{w}}^{\max} = 0.01$, no rheological healing, $\lambda_{660} = 20$) over 5 billion years of model time. The video consists of six panels, each showing a different field: **(a)** basalt fraction, **(b)** material age (time since material last underwent a melting episode), **(c)** tempera-

ture, **(d)** viscosity, **(e)** detected mantle domain field (see Text S3), and **(f)** strain field. Even though SW rheology operates in the modelled lower mantle, the model shows a similar thermal evolution and final viscosity profile as the reference model M_0 (see Fig. S5) due to the increased viscosity jump in the lower-mantle (λ_{660}). Strain localization still occurs in mantle plumes and thermochemical piles, and their dynamics are different than those in the reference model (see Text S4).

References

Arnould, M., Coltice, N., Flament, N., & Mallard, C. (2020). Plate tectonics and mantle controls on plume dynamics. *Earth and Planetary Science Letters*, *547*, 116439. Retrieved from https://doi.org/10.1016/j.epsl.2020.116439 doi: 10.1016/j.epsl.2020.116439

Crameri, F. (2018). Geodynamic diagnostics, scientific visualisation and StagLab 3.0. *Geoscientific Model Development*, *11*(6), 2541–2562. doi: 10.5194/gmd-11-2541-2018

Forte, A. M., & Mitrovica, J. X. (1996). New inferences of mantle viscosity from joint inversion of long-wavelength mantle convection an post-glacial rebound data. *Geophysical Research Letters*, *23*(10), 1147–1150.

Fuchs, L., & Becker, T. W. (2019). Role of strain-dependent weakening memory on the style of mantle convection and plate boundary stability. *Geophysical Journal International*, *218*(1), 601–618. doi: 10.1093/gji/ggz167

Hassan, R., Flament, N., Gurnis, M., Bower, D. J., & Müller, D. (2015). Provenance of plumes in global convection models. *Geochemistry Geophysics Geosystems*, *16*(1), 267–300. Retrieved from https://doi.org/10.1002/2014GC005606 doi: 10.1002/2014GC005684.Key

Labrosse, S. (2002). Hotspots, mantle plumes and core heat loss. *Earth and Planetary Science Letters*, *199*(1-2), 147–156. doi: 10.1016/S0012-821X(02)00537-X

Lau, H. C., Mitrovica, J. X., Austermann, J., Crawford, O., Al-Attar, D., & Latychev, K. (2016). Inferences of mantle viscosity based on ice age data sets: Radial structure. *Journal of Geophysical Research: Solid Earth*, *121*(10), 6991–7012. doi: 10.1002/2016JB013043

McKenzie, D. (1979). Finite deformation during fluid flow. *Geophys. J. R. astr. Soc.*, *58*, 689–715.

Mitrovica, J. X., & Forte, A. M. (2004). A new inference of mantle viscosity based upon joint inversion of convection and glacial isostatic adjustment data. *Earth and Planetary Science Letters*, *225*(1-2), 177–189. doi: 10.1016/j.epsl.2004.06.005

Peltier, W. R. (1996). Mantle viscosity and ice-age ice sheet topography. *Science*, *273*(5280), 1359–1364. doi: 10.1126/science.273.5280.1359

Schierjott, J., Rozel, A., & Tackley, P. J. (2020). On the self-regulating effect of grain size evolution in mantle convection models: Application to thermochemical piles. *Solid Earth*, *11*(3), 959–982. doi: 10.5194/se-11-959-2020

Steinberger, B., & Calderwood, A. R. (2006). Models of large-scale viscous flow in the Earth's mantle with constraints from mineral physics and surface observations. *Geophysical Journal International*, *167*(3), 1461–1481. doi: 10.1111/j.1365-246X .2006.03131.x

Steinberger, B., & Holme, R. (2008). Mantle flow models with core-mantle boundary constraints and chemical heterogeneities in the lowermost mantle. *Journal of Geophysical Research: Solid Earth*, *113*(5), 1–16. doi: 10.1029/2007JB005080

Tackley, P. J. (2000a). Self-consistent generation of tectonic plates in three-dimensional mantle convection 1. pseudoplastic yielding. *Geochemistry, Geophysics, Geosystems*, *1*(1), 9–22. doi: 10.1016/S0012-821X(98)00029-6

Tackley, P. J. (2000b). Self-consistent generation of tectonic plates in time-dependent, three-dimensional mantle convection simulations 2. strain weakening and asthenosphere. *Geochemistry, Geophysics, Geosystems*, *1*. doi: 10.1029/2000gc000036

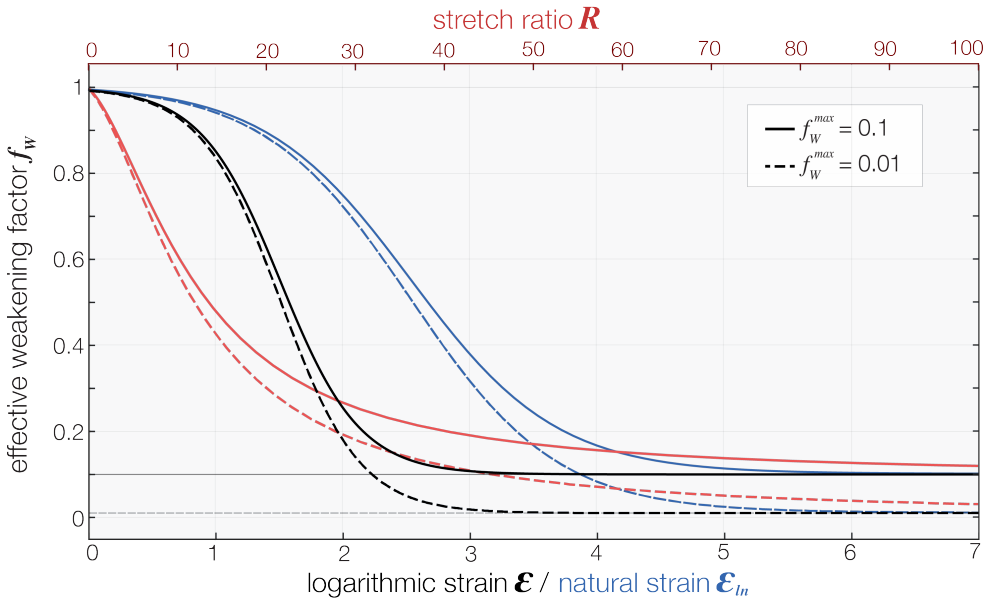

Figure S1. Same weakening curve employing different projections: (black) As a function of logarithmic strain ($\varepsilon = log_{10}(a/b)$ - as used in the main text), (blue) natural strain ($\varepsilon_{ln} = ln(a/b)$) and (red) the stretch ratio ($R = a/b$).

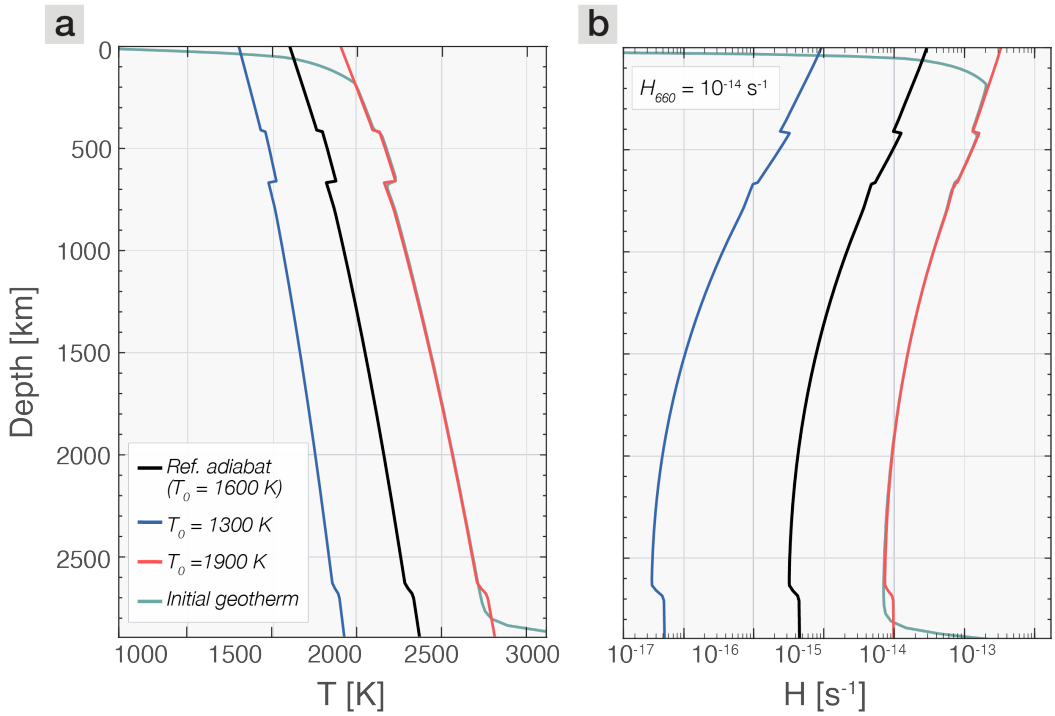

Figure S2. **(a)** reference adiabat with $T_0 = 1600$ K, and shifted +300 K and −300 K, and the initial geotherm of the model. **(b)** resulting healing rate profiles based on eq. (6) in the main text, with reference healing rate at 660 km depth: $H_{660} = 10^{-15}$ s^{-1}.

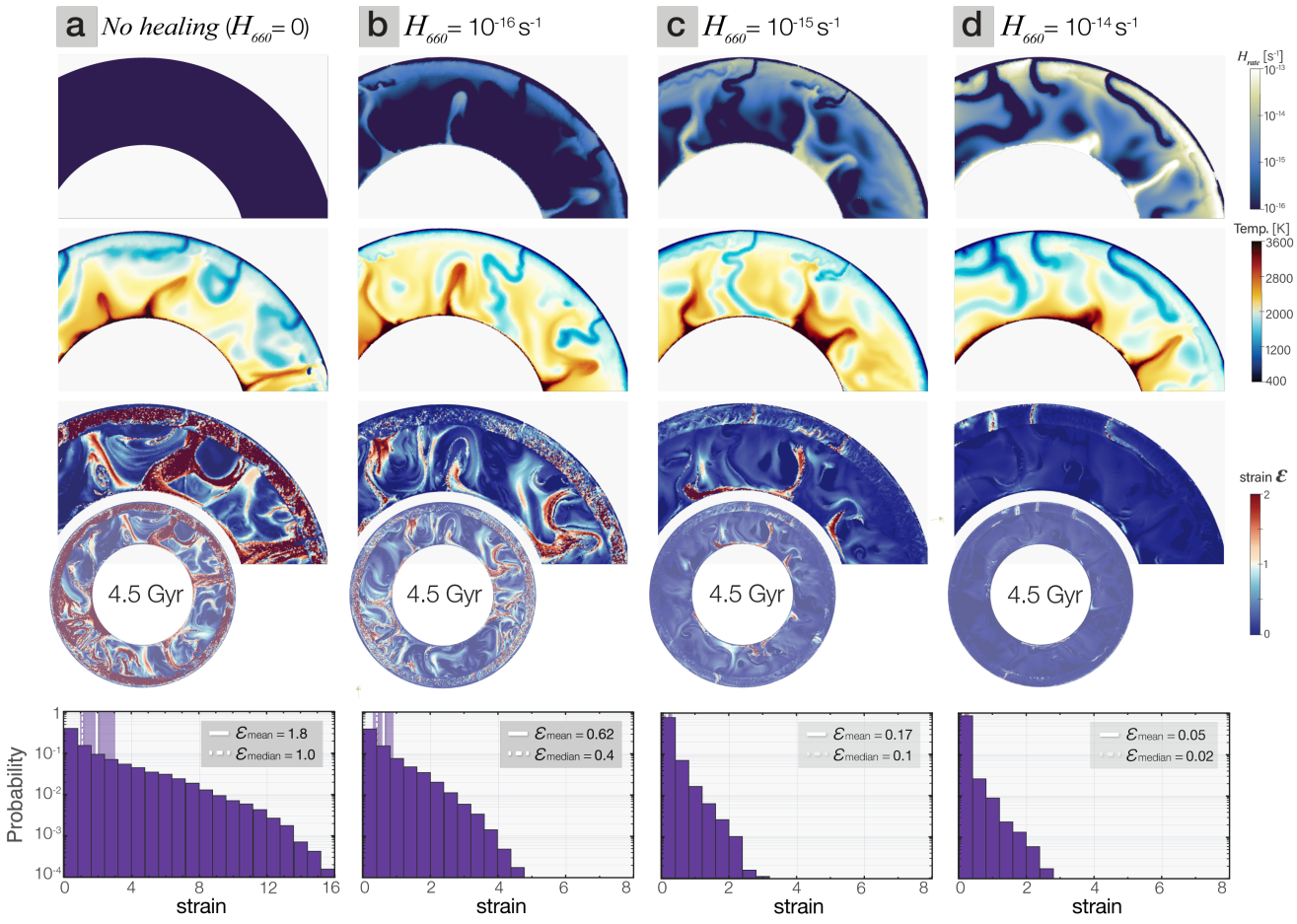

Figure S3. Final snapshots of models with, from left to right, an increasing rheological healing rate of strain. **(a)** shows the reference model (zero strain weakening and zero rheological healing). Panels **(b-d)** show models with no strain weakening rheology, but increasing healing rate (H_{660}) values: 10^{-16} s^{-1}, 10^{-15} s^{-1}, and 10^{-14} s^{-1}, respectively. These different healing rates affect the strain field significantly. Since no strain weakening is applied in these models, the differences in healing rates do not affect model evolution. Top row: healing rate, second row: temperature, third row: strain, fourth row: strain histogram (vertical lines represent the mean and median values for each histogram).

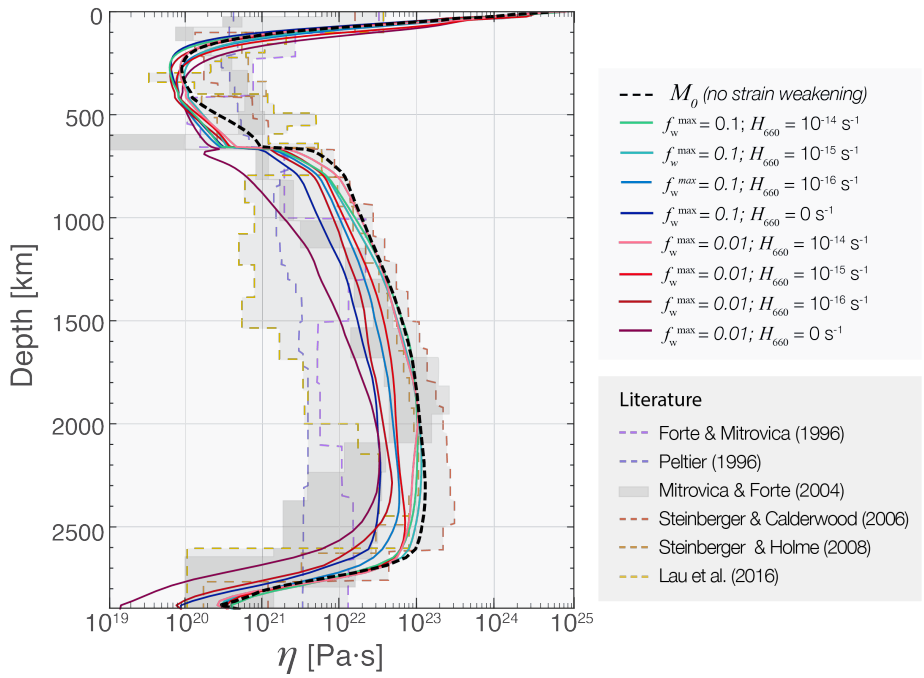

Figure S4. Solid lines: final averaged viscosity profiles of all main models in this study. Dotted lines: several radial viscosity profiles for Earth from previous studies, inferred from post-glacial rebound data (Peltier, 1996; Lau et al., 2016); joint post-glacial rebound and convection data (Forte & Mitrovica, 1996; Mitrovica & Forte, 2004); joint mineral physics and surface observations (Steinberger & Calderwood, 2006); joint mineral physics, surface observations, and convection data (Steinberger & Holme, 2008).

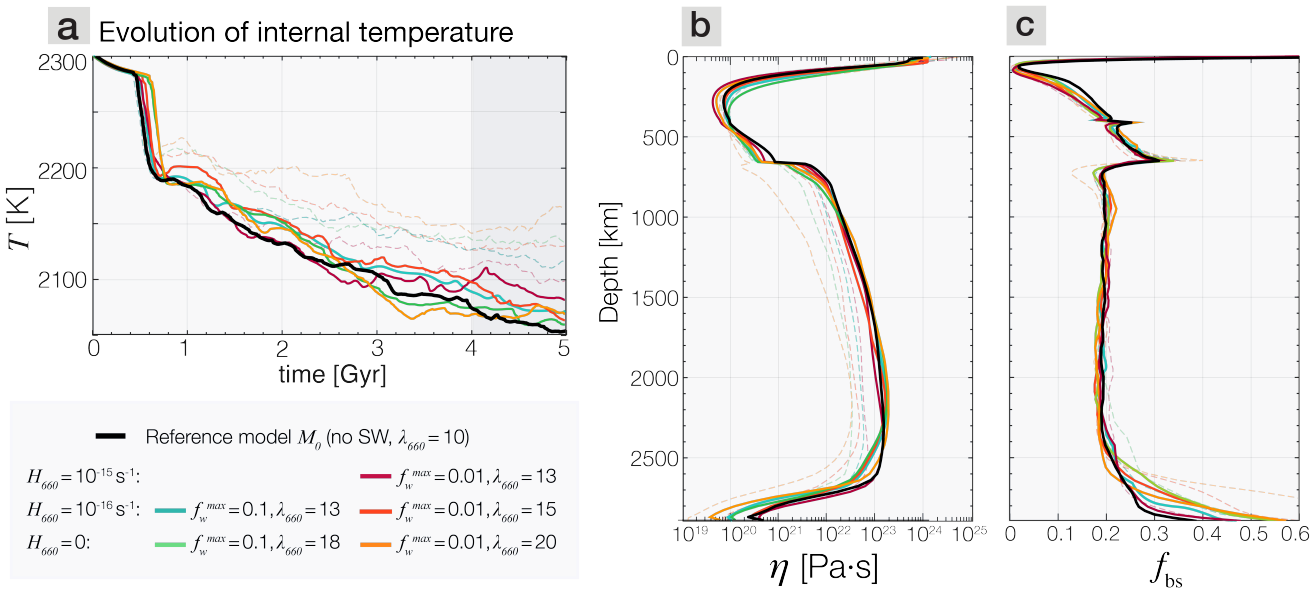

Figure S5. **a)** Temporal evolution of internal temperature for reference model case (black line) and additional SW cases (color-coded) with variable weakening + healing scenarios and an increased lower mantle viscosity jump. **(b)** All of these cases display a similar final lower mantle viscosity profile. Panel **(c)** shows the basalt radial profiles. The radial profiles are averaged between 4 and 5 Gyr. The dashed lines are the SW models corresponding to the additional cases but with λ_{660}=10.

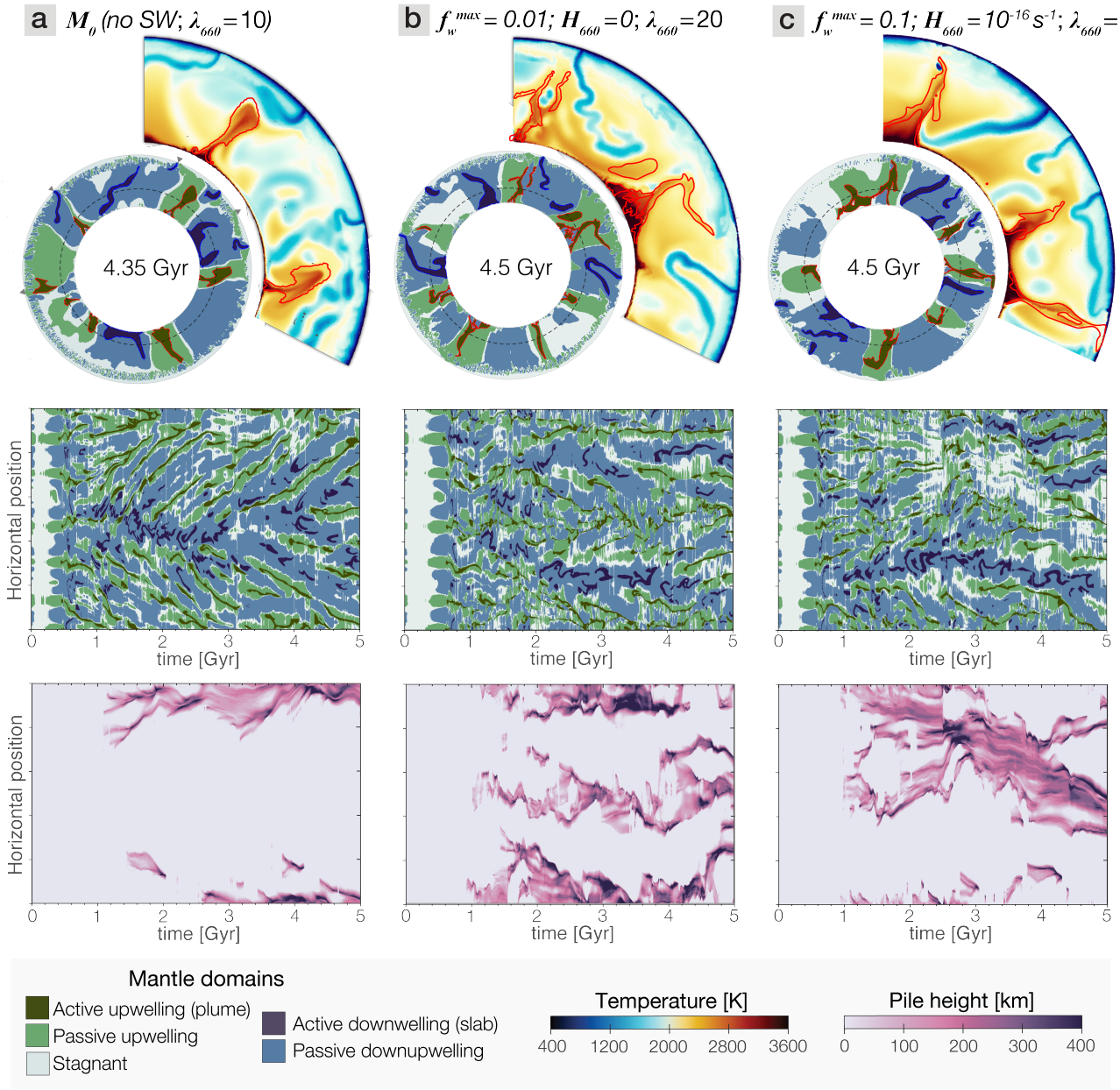

Figure S6. Top: age-of-the-Earth snapshots for three selected models showing the mantle domain field. Red outline: active mantle upwellings, blue outline: active mantle downwellings. Zoom-ins show the temperature field. Bottom: temporal evolution of the lateral distribution of the mantle domain field at 1800 km depth. See Section 2.5 in the main text for the definitions of the mantle domains. Bottom: temporal evolution of the lateral distribution of detected thermochemical piles atop the core-mantle boundary, color-coded according to the height of the detected pile. **(a)** Reference model: neither SW rheology nor rheological healing. **(b)** Additional case with strain-weakening, no rheological healing and an increased viscosity jump at the 660 boundary (λ_{660}). **(c)** Additional case with SW rheology and healing simultaneously activated, as well as an increased λ_{660}. See Text S4 for more details regarding these additional cases.

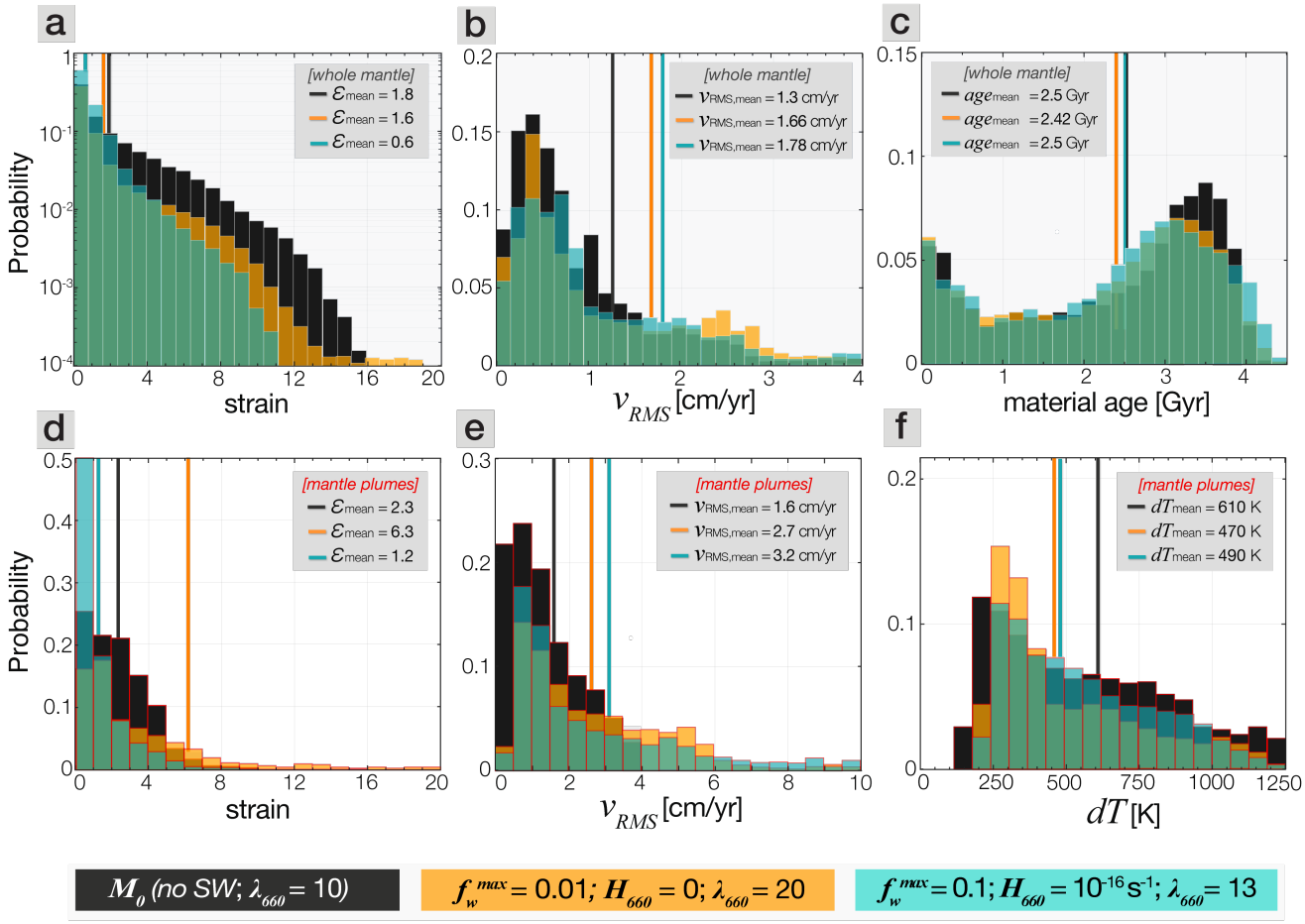

Figure S7. Histograms of selected quantities for selected models: the reference model M_0 (black) and two additional cases with variable combinations of strain-weakening and healing plus an increased viscosity jump (λ_{660}) at the 660 km discontinuity (orange, blue). The colour scheme corresponds to that in Figure 6 in the main text, with the difference being the higher viscosity jump in the additional cases explored here. See Text S4 for details. **(a-c)** Distribution of the strain field, the root mean-square velocity, and the material age within the whole mantle domain. **(d-f)** Distribution of the strain field, the root mean-square velocity, and the average horizontal temperature anomaly of the material within the detected active mantle upwellings (plumes). The vertical lines represent the mean values for each histogram.

Table S1. Model parameter summary and output quantities of all models run in this study, time-averaged between 4.0 and 5.0 Gyr of model evolution. Subscript $_{\mathrm{m}}$ stands for the average in the whole mantle (weighted by the volume of each cell). p and m stand for Plateness and Mobility, respectively (Tackley, 2000a). ϵ represents strain, T the temperature, v_{RMS} the root-mean-square velocity, Nu_{top} and Nu_{bot} the top and bottom Nusselt number, respectively. F_{top} and F_{bot} are the top and bottom heat flux, age is the age of the mantle material (time since it last underwent a melting episode), and $Pile_{\mathrm{vol}}$ is the mantle volume percentage occupied by detected thermochemical piles.

Model	$f_{\mathrm{w}}^{\mathrm{max}}$	H_{660} [s^{-1}]	λ_{660}	p	m	ε_{m}	T_{m} [K]	η_{m} [Pa·s]	$v_{\mathrm{RMS,m}}$ [cm/yr]	Nu_{bot}	Nu_{top}	F_{top} [TW]	F_{bot} [TW]	age [Gyr]	$Pile_{\mathrm{vol}}$ [$\mathrm{vol}_{\mathrm{mantle}}$%]
M_0	0	0	10	0.96	1.8	1.6	2042	$1.2{\cdot}10^{24}$	1.31	17	13	22	28	2.5	0.6
M_{01}	0.1	0	10	0.97	1.6	2.2	2108	$1.0{\cdot}10^{24}$	1.97	24	13.8	25	40	2.5	1.7
M_{001}	0.01	0	10	0.97	1.3	2.8	2132	$9.2{\cdot}10^{23}$	2.41	27	13.6	25	44	2.6	2.2
$M_{01\mathrm{H}16}$	0.1	10^{-16}	10	0.97	1.6	0.6	2102	$1.1{\cdot}10^{24}$	1.47	18	12	23	31	2.5	1.4
$M_{001\mathrm{H}16}$	0.01	10^{-16}	10	0.97	1.6	0.8	2104	$1.0{\cdot}10^{24}$	1.90	23	13.2	25	40	2.6	1.8
$M_{01\mathrm{H}15}$	0.1	10^{-15}	10	0.97	1.6	0.4	2063	$1.2{\cdot}10^{24}$	1.50	20	12.6	23	36	2.4	1.2
$M_{001\mathrm{H}15}$	0.01	10^{-15}	10	0.97	1.6	0.6	2090	$1.1{\cdot}10^{24}$	1.68	21	12.6	24	34	2.5	1.4
$M_{01\mathrm{H}14}$	0.1	10^{-14}	10	0.97	1.6	0.2	2072	$1.2{\cdot}10^{24}$	1.34	18	12.7	23	31	2.5	0.8
$M_{001\mathrm{H}14}$	0.01	10^{-14}	10	0.97	1.5	0.3	2065	$1.2{\cdot}10^{24}$	1.38	22	13.3	25	38	2.6	1.1
$M_{01\lambda}{}^{*}$	0.1	0	18	0.97	1.6	1.6	2060	$1.2{\cdot}10^{24}$	1.56	20	12.7	24	35	2.5	1.0
$M_{001\lambda}{}^{*}$	0.01	0	20	0.97	1.4	1.8	2061	$1.2{\cdot}10^{24}$	1.82	21	13	25	40	2.4	1.1
$M_{01\mathrm{H}16\lambda}{}^{*}$	0.1	10^{-16}	13	0.97	1.4	0.6	2077	$1.2{\cdot}10^{24}$	1.63	19	12.6	23	29	2.5	1.0
$M_{001\mathrm{H}16\lambda}{}^{*}$	0.01	10^{-16}	15	0.97	1.4	0.7	2080	$1.2{\cdot}10^{24}$	1.77	18	13.2	23	33	2.4	1.0
$M_{001\mathrm{H}15\lambda}{}^{*}$	0.01	10^{-15}	13	0.97	1.5	0.4	2093	$1.2{\cdot}10^{24}$	1.48	20	12.3	23	31	2.5	0.8

* Additional cases with $\lambda_{660} > 10$, see Text S4 and Figures S5-S7.

Table S2. Summary of average quantities within detected mantle plumes ($_{\mathrm{pl}}$) in the models, time-averaged between 4.0 and 5.0 Gyr of model evolution. ϵ stands for the strain, dT the horizontal temperature anomaly, v_{RMS} the root-mean-square velocity, F the heat flux carried by the plumes at 1800 km depth (middle of the lower mantle), and T_{660} the temperature of the plumes detected at 660 km depth (just below the mantle transition zone).

Model	$f_{\mathrm{w}}^{\mathrm{max}}$	H_{660} [s^{-1}]	λ_{660}	$\varepsilon_{\mathrm{pl}}$	dT_{pl} [K]	$v_{\mathrm{RMS,pl}}$ [cm/yr]	F_{pl} [TW]	$T_{pl,660}$ [K]
M_0	0	0	10	2.3	610	1.4	18	1905
M_{01}	0	0.1	10	6.2	400	1.71	22	1991
M_{001}	0	0.01	10	8.5	420	1.88	24	2075
$M_{01\mathrm{H16}}$	0.1	10^{-16}	10	2.0	400	2.3	26	2031
$M_{001\mathrm{H16}}$	0.01	10^{-16}	10	2.4	431	2.5	27	2057
$M_{01\mathrm{H15}}$	0.1	10^{-15}	10	1.6	508	1.6	22	1977
$M_{001\mathrm{H15}}$	0.01	10^{-15}	10	1.9	447	1.8	24	1996
$M_{01\mathrm{H14}}$	0.1	10^{-14}	10	1.4	560	1.5	21	1949
$M_{001\mathrm{H14}}$	0.01	10^{-14}	10	1.6	522	1.7	22	1968
$M_{01\lambda}{}^*$	0.1	0	10	5.2	502	2.3	26	1985
$M_{001\lambda}{}^*$	0.01	0	10	6.3	470	2.7	29	2016
$M_{01\mathrm{H16}\lambda}{}^*$	0.1	10^{-16}	10	1.2	490	3.2	25	2009
$M_{001\mathrm{H16}\lambda}{}^*$	0.01	10^{-16}	10	1.4	460	3.3	24	2029
$M_{001\mathrm{H15}\lambda}{}^*$	0.01	10^{-15}	10	1.0	500	3.0	23	1993

* Additional cases with $\lambda_{660} > 10$, see Text S4 and Figures S5-S7.